Journal of Molecular Liquids 394 (2024) 123746

Contents lists available at ScienceDirect

Journal of Molecular Liquids

journal homepage: www.elsevier.com/locate/molliq

Hydrophobicity as the key to understanding the nanostructural behavior of eutectic mixtures upon apolar cosolvent addition

Giorgia Mannucci, Alessandro Tofoni, Matteo Busato *, Paola D'Angelo *

Department of Chemistry, University of Rome "La Sapienza", P.le A. Moro 5, Rome, 00185, Italy

ARTICLE INFO

Keywords:
Nanostructure
Hydrophobic deep eutectic solvents
Menthol
Butylated hydroxytoluene
Thymol
Hexane
Molecular dynamics
X-ray scattering

ABSTRACT

The influence of the addition of the apolar *n*-hexane (HEX) cosolvent on the structural arrangement of eutectic mixtures with different degrees of hydrophobicity, namely butylated hydroxytoluene (BHT), L-menthol (MEN), thymol (TYM), and choline chloride (ChCl), has been studied with a combined approach using small- and wide-angle X-ray scattering and molecular dynamics simulations. The cosolvent introduction has a similar impact on the molecular scale-length aggregation in BHT:MEN:HEX, TYM:MEN:HEX, and ChCl:TYM:HEX mixtures at different 1:3:H, 1:2:H, and 1:7:H molar ratios, specifically a dramatic perturbation of the main interactions present in the pure eutectics where hydrogen-bonds dominate. On larger scale-lengths, HEX addition results in a homogeneous electron-density distribution in the BHT:MEN:HEX and TYM:MEN:HEX mixtures due to a high affinity of the cosolvent for the BHT, MEN, and TYM components. Conversely, the presence of the more hydrophilic ChCl compound in the ChCl:TYM 1:7 system is the driving force for the segregation mechanism of this component which causes the formation of nano-scale inhomogeneities at high HEX concentrations, before macroscopic phase separation. The different degree of hydrophobicity is therefore key to understanding the nanostructural behavior of these eutectics in the presence of an apolar cosolvent. These findings have important implications for the employment of deep eutectic solvent mixtures, as the formation of pseudo-phase aggregates can help explaining the macroscopic behavior of these alternative media in applications like extraction procedures.

1. Introduction

Deep eutectic solvents (DESs) are mixtures of two or more compounds showing a melting point depression that is deeper than the ideally predicted one at specific molar ratios. [1] As a result, the melting point of the mixture is lower than those of the parent constituents, so that a fluid phase at room temperature can be obtained even from solid starting materials. The origin of such a thermal behavior lies in packing hampering, asymmetric ions, and strong interactions between the components, often consisting of hydrogen-bonding (H-bonding). [2–5] In recent years, DESs gained a lot of interest owing to peculiar properties like high conductivity, undetectable volatility, non-flammability, and low toxicity. [6–8] DESs are usually classified into five categories according to the chemical nature of the components, and the majority of these eutectics falls into the so-called "type I - IV" categories, being formed by at least one ionic compound. [8] However, differently from other alternative solvents like ionic liquids (ILs), it is not necessary for DESs to contain ions, and the "type V" category has been more recently proposed. [9,10] This class is formed by neutral molecular components only, very often based on terpenoid compounds, as in the case of the prototypical "type V" eutectic formed by thymol (THY) and L-menthol (MEN). [11,12] As non-ionic solvents, these DESs often show lower viscosity, are chloride-free, and hydrophobic, properties which enhance their use as extracting phases for the removal of lipophilic compounds from aqueous solutions. [10,13] The benefits of DESs over traditional solvents also consist in their inherently tunable nature, meaning that their physical-chemical properties can be designed to achieve specific requirements through careful selection of the constituents and/or their molar ratio. [7] Besides direct action on the constituents, cosolvent addition has been found as a further strategy to obtain eutectics with enhanced performances at lower costs. [14,15] For example, cosolvents are added as dispersing agents in extraction procedures to lower the often high viscosity of these eutectics. [16–18] In this light, the introduction of an additional species such as water, alcohols, or alkanes in an eutectic mixture can seriously affect its key properties like density, viscosity, conductivity, extraction efficiency, and enzyme activity. [19–25]

* Corresponding author.
E-mail addresses: matteo.busato@uniroma1.it (M. Busato), p.dangelo@uniroma1.it (P. D'Angelo).

https://doi.org/10.1016/j.molliq.2023.123746
Received 18 September 2023; Received in revised form 17 November 2023; Accepted 5 December 2023
Available online 10 December 2023

A unique feature of DESs is also a distinct bulk nanostructure, resulting from the concurrence of several intra- and inter-molecular interactions due to coulomb and dispersion forces, H-bonding, and steric exclusions. [26,27] In this framework, cosolvent addition has turned out to also alter DESs nanostructure in peculiar and often unpredictable ways. For example, aqueous mixtures of the hydrophilic choline chloride (ChCl):urea 1:2 DES have been explored by means of neutron diffraction and empirical structure potential refinement, showing that the DES nanostructure is maintained up to remarkably high water contents. [28] The same approach was employed to investigate water/malicine (ChCl:malic acid 1:1) mixtures, evidencing the formation of worm-like structures at low water concentrations. [29] On the other hand, a combined X-ray scattering, infrared spectroscopy, and molecular dynamics (MD) simulation investigation has detected the presence of nanoscale structures in aqueous mixtures of the *quasi*-hydrophobic ChCl:sesamol 1:3 mixture. [30,31] Here, water pools of ~70 Å dimensions rich in ChCl result from sesamol segregation, while simultaneously not provoking macroscopic phase separation. [30] Interestingly, analogous mixtures with methanol showed the formation of no such structures at the nano-scale level. [32] Therefore, the alteration induced by cosolvent addition to a DES appears highly system-dependent. As the nanostructure can significantly influence the physical-chemical properties and thus the potential applications of DESs, it is essential to understand the underlying factors governing these solvent properties.

Here, we tackle some of these unanswered questions with a study on the butylated hydroxytoluene (BHT):MEN, TYM:MEN, and ChCl:TYM mixtures in the presence of the apolar cosolvent *n*-hexane (HEX) at different 1:3:*H*, 1:2:*H* and 1:7:*H* molar ratios. The molecular structures of the components are shown in Fig. 1. The peculiarity of these systems is the decreasing hydrophobicity going from BHT:MEN 1:3 to TYM:MEN 1:2 and ChCl:TYM 1:7. [33–35] While the TYM:MEN 1:2 mixture is considered as the archetypal "type V" hydrophobic DES, [12,35] the BHT:MEN 1:3 eutectic has recently shown interesting properties as receiving phase for the extraction of fat-soluble micronutrients and pesticides from food matrices, besides showing an antioxidant activity guaranteed by the BHT component. [36,37] Although highly hydrophobic, a recent study has shown that the addition of polar cosolvents such as methanol and ethanol is able to disrupt the most relevant interactions present in this eutectic. [34] On the other hand, the ChCl:TYM 1:7 system is interesting because of the unusually high molar ratio of TYM, which is only moderately soluble in water, with respect to the hydrophilic ChCl component. Moreover, to the best of our knowledge, this mixture has only been presented in the 1:4 molar ratio so far. [38] Consequently, it is of great interest to evaluate the influence of an apolar cosolvent on these eutectic mixtures with different degrees of hydrophobicity. Increasing molar ratios of HEX will be studied to investigate how the cosolvent concentration influences the structural arrangement of the pristine systems on different scale-lengths, spanning from molecular- to nano-scale aggregation. To this purpose, we employed a combined approach using X-ray scattering both in the small- (SAXS) and wide-angle (WAXS) regime together with MD simulations. So far, MD simulations have been profitably used to give detailed interpretations of experimental data regarding complex systems like DESs, given their ability to deliver information from the molecular length-scale to the macroscopic behavior. [2,39–46] On the other hand, previous experimental studies about DES nanostructure have largely focused on scattering techniques, in particular when successfully validated by computational outcomes. [26–28,30,32,47,31]

2. Materials and methods

2.1. Chemicals and sample preparation

BHT (food grade, ⩾ 99%), MEN (natural source, food grade, ⩾ 99%), TYM (⩾ 99%), ChCl (⩾ 99%), and HEX (⩾ 99%) were purchased from Sigma-Aldrich. In order to remove water traces ChCl was dried at 110 °C for 12 hours in a muffle oven. The BHT:MEN 1:3, TYM:MEN 1:2, and ChCl:TYM 1:7 liquid phases were prepared by mixing the components at the required molar ratio in glass test tubes and then heating at 323 K until homogeneous transparent liquids were obtained. Precise amounts of the HEX cosolvent were added to these eutectics to obtain BHT:MEN:HEX, TYM:MEN:HEX, and ChCl:TYM:HEX mixtures at different 1:3:*H*, 1:2:*H*, and 1:7:*H* molar ratios, with *H* comprised in the 1 - 26 range.

2.2. SWAXS measurements

Small- and wide-angle X-ray scattering (SWAXS) spectra were collected using a Dectris Pilatus3 1M detector with an automatic sample changer at the Austrian SAXS beamline of the Elettra Synchrotron (Trieste, Italy). [48] All measurement were performed at room temperature on the BHT:MEN:HEX, TYM:MEN:HEX and ChCl:TYM:HEX mixtures at different 1:3:*H*, 1:2:*H* and 1:7:*H* molar ratios with $H = 1 - 26$. A silver behenate standard was used to calibrate the scattering vector q range. An overall explored q region of 0.05 - 1.8 $Å^{-1}$ was obtained as a result of measurements with different sample-detector distances. The IGOR Pro software (IGOR Pro 7.0.8.1, Wavemetrics) was used to subtract the two-dimensional scattering patterns for the dark counts, and then to mask, azimuthally average, and normalize for transmitted beam intensity, exposure time, and subtended solid angle *per* pixel. Using the SAXSutilities2 tool [49] the empty capillary contributions were subtracted and the different angular ranges were merged.

2.3. MD simulations

Classical MD simulations were performed on BHT:MEN:HEX, TYM:MEN:HEX and ChCl:TYM:HEX systems at different 1:3:*H*, 1:2:*H* and 1:7:*H* molar ratios. Periodic cubic boxes with ~50 Å side lengths and a number of species chosen to reproduce the density of each mixture were built by randomizing the initial atomic positions with the PACKMOL package. [50] For the BHT:MEN:HEX 1:3:*H*, TYM:MEN:HEX 1:2:*H* and ChCl:TYM:HEX 1:7:*H* systems with $H = 12$ and 26, simulations were also carried out on ~100 Å side boxes to inspect the formation of larger-size inhomogeneities (*vide infra*). Details about the studied systems are reported in Tables S1, S2, and S3 of the Supplementary Material. Structures and interactions of the BHT, TYM, and HEX molecules were represented by the all-atom optimized potentials for liquid simulations (OPLS-AA) force field, [51] while OPLS-compatible parameters developed by Canongia Lopes and Padua have been employed for the cholinium cation [52] and for the chloride anion. [53] For the MEN molecule the OPLS-compatible parameters developed by Jasik et al. [54] were employed. The long-range electrostatic forces were calculated with the particle mesh Ewald method and a cutoff radius of 12 Å was chosen for all the non-bonded interactions. [55,56] Cross-terms for the Lennard-Jones interactions were constructed with the Lorentz-Berthelot combining rules. The systems were equilibrated in the NVT ensemble with a heating ramp from 300 to 700 K (10 ns), and then cooled down to 300 K for a total time of 20 ns. Slow dynamics systems such as ILs and DESs have been shown to require high temperature equilibrations. [39,57–61] Production runs for data analysis were carried out in NVT conditions at 300 K for 50 ns. The temperature was controlled with the Nosé-Hoover thermostat with a relaxation constant of 0.5 ps. The leap-frog algorithm was used to integrate the equation of motion with a time step of 1 fs. The LINCS algorithm, instead, was employed to constrain all the stretching vibrations involving the hydrogen atoms. [62] All the simulations and the analyses were performed with the Gromacs 2020.6 program, [63] with the exception of the Voronoi tessellation analysis [64] that was carried out with the TRAVIS package. [65] Scattering profiles were calculated from the MD trajectories using the gmx saxs Gromacs tool, which employs Cromer's method to calculate SAXS structure factors for a given system. [66] For the BHT:MEN:HEX 1:3:*H* and TYM:MEN:HEX 1:2:*H* systems, with *H*

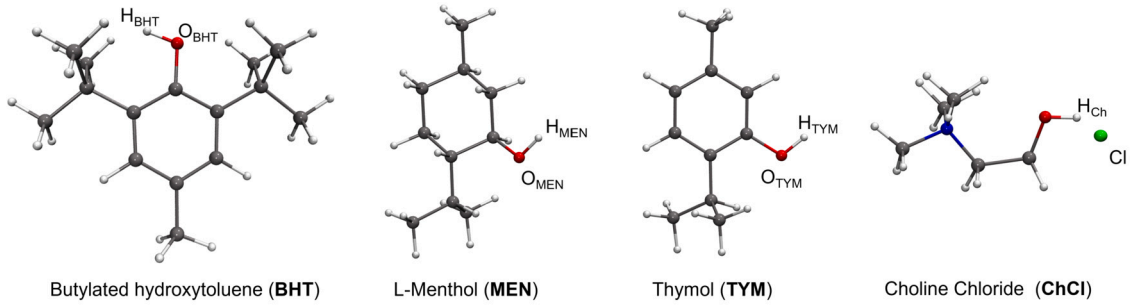

Fig. 1. Molecular structures of butylated hydroxytoluene (BHT), L-menthol (MEN), thymol (TYM), and choline chloride (ChCl) showing the employed atom nomenclature (white, hydrogen; gray, carbon; blue, nitrogen; red, oxygen; green, chloride).

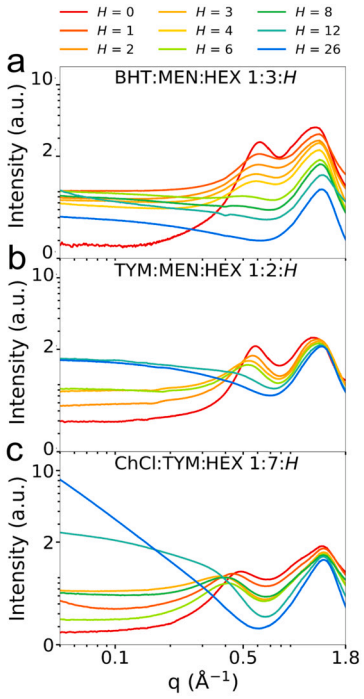

Fig. 2. Experimental SWAXS spectra collected on the a) BHT:MEN:HEX, b) TYM:MEN:HEX, and c) ChCl:TYM:HEX mixtures at different 1:3:*H*, 1:2:*H*, and 1:7:*H* molar ratios.

equal to 12 and 26, the SWAXS profiles were calculated from the MD trajectories using the TRAVIS package. [65] The VMD 1.9.3 software was used for trajectories visualization. [67]

3. Results and discussion

3.1. Detection of different scale-length aggregation: SWAXS results

The SWAXS data collected on the BHT:MEN:HEX, TYM:MEN:HEX, and ChCl:TYM:HEX mixtures at different 1:3:*H*, 1:2:*H*, and 1:7:*H* molar ratios, respectively, are shown in Fig. 2. The experimental spectra show a common feature among the three systems, that is the presence of a double peak in the WAXS region ($q > \sim 0.5$ Å^{-1}). This contribution was previously detected for "type V" DESs and deemed diagnostic of the H-bonding aggregation among terpenoid compounds. [68,12,33,34] Indeed, the WAXS pre-peak in the BHT:MEN 1:3, TYM:MEN 1:2, and ChCl:TYM 1:7 pristine eutectics that is detectable in the 0.48 - 0.63 Å^{-1} region (Fig. 2 for $H = 0$) corresponds to distances in the real space of 10.30 - 13.52 Å. This interval well reflects the recurring distances among pools of interacting hydroxyl groups (electron density-rich regions) intercalated by the carbon bodies of the constituents (electron density-poor regions), acting as a sort of molecular spacers. In this framework, the experimental evidence is that this contribution is found to broaden and shift to lower q-values (thus to longer distances in the real space) upon HEX addition, indicating that the added cosolvent is somehow able to perturb the molecular aggregation present in the pristine eutectics. It is worth noting that the flattening trend is particularly pronounced for the BHT:MEN:HEX 1:3:*H* mixtures, which barely show the presence of a WAXS pre-peak already for the $H = 6$ sample, while a higher preservation of the double-peak feature is displayed by the TYM:MEN:HEX and ChCl:TYM:HEX systems, albeit a marked shift towards lower q-values.

Moving to the small-angle region ($q < \sim 0.5$ Å^{-1}), the striking outcome is a different spectral evolution of the three systems upon HEX addition. The low-q region is sensitive towards electron density inhomogeneities on larger scale-lengths, [26,27,30,32] and therefore points to a different behavior of the eutectic nanostructure upon cosolvent addition. In particular, the rise in the small-angle scattered intensity becomes sequentially more relevant following the BHT:MEN < TYM:MEN < ChCl:TYM trend. Interestingly, this sequence also reflects the lowering in hydrophobicity across these solvents. A rather flat small-angle region is shown by the BHT:MEN:HEX (Fig. 2a) and TYM:MEN:HEX (Fig. 2b) systems even for high HEX concentrations, while a marked increase of the scattered intensity is observed for the ChCl:TYM:HEX 1:7:12 and 1:7:26 samples (Fig. 2c). Inspection of the macroscopic aspect of these systems can help addressing the nature of such inhomogeneities. In Figure S1 we show pictures of the analyzed samples for the highest HEX concentrations. Here, it can be noticed that the BHT:MEN:HEX 1:3:*H* (Figure S1a) and TYM:MEN:HEX 1:2:*H* (Figure S1b) mixtures appear as homogeneous transparent liquids even at very high HEX molar ratios. On the other hand, while the $H = 12$ sample for the ChCl:TYM:HEX 1:7:*H* mixtures appears homogeneous as well, the $H = 26$ one shows a cloudy aspect (Figure S1c). This indicates that HEX is no more soluble in the DES after this threshold, an indirect proof that, while the marked rise of the small-angle scattered intensity in the $H = 26$ sample is due to macroscopic phase separation, that observed for the $H = 12$ mixture must relate to electron density inhomogeneities occurring at a microscopic scale-length. The nature of such inhomogeneities and their system-dependency are the subject of the following discussion.

3.2. MD simulation analysis

To find a rationale for the different spectral behavior shown by the three eutectics upon HEX addition, MD simulations were carried out on BHT:MEN:HEX, TYM:MEN:HEX, and ChCl:TYM:HEX mixtures at different 1:3:*H*, 1:2:*H*, and 1:7:*H* molar ratios. A first qualitative evaluation of the extent of aggregation among the different components can be obtained looking at the snapshots taken from the simulation boxes. Concerning the low HEX content, in Figure S2 we show as an example snapshots for the $H = 3$ mixtures, while those for the $H = 12$ (Fig. 3) and $H = 26$ (Fig. 4) systems allow us to gain a first insight into the behavior of the mixtures in the presence of high HEX concentrations. Here, both the BHT:MEN:HEX 1:3:*H* and TYM:MEN:HEX 1:2:*H*

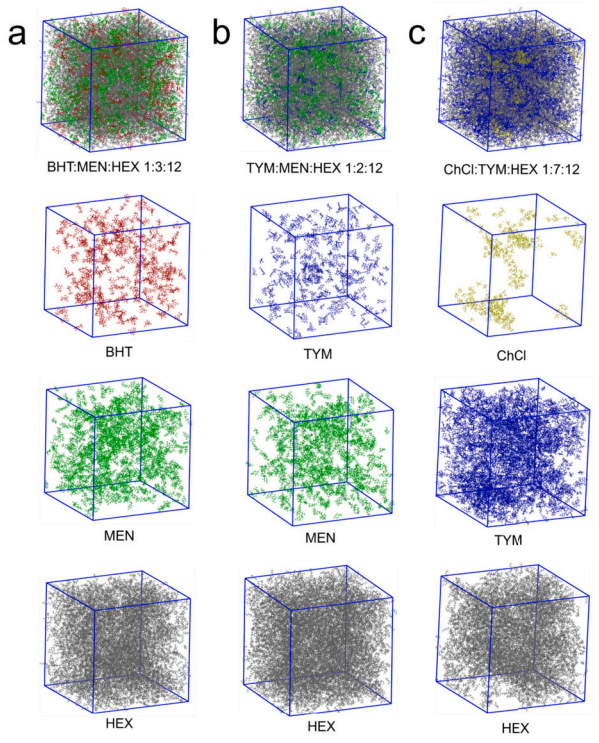

Fig. 3. Snapshots taken from the final configurations of the MD simulations for the a) BHT:MEN:HEX, b) TYM:MEN:HEX, and c) ChCl:TYM:HEX mixtures at 1:3:12, 1:2:12, and 1:7:12 molar ratios, respectively. Separate illustrations are shown for the entire system and for the different components (red, BHT; green, MEN; blue, TYM; yellow, ChCl; gray, HEX).

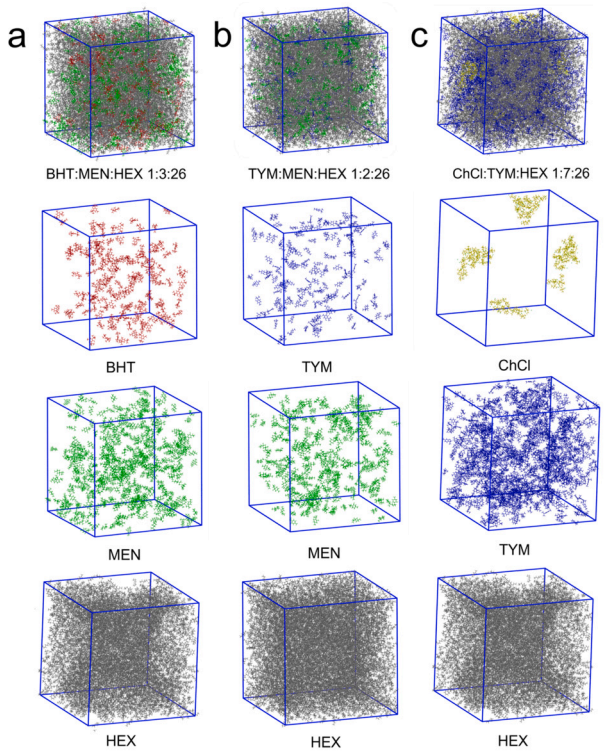

Fig. 4. Snapshots taken from the final configurations of the MD simulations for the a) BHT:MEN:HEX, b) TYM:MEN:HEX, and c) ChCl:TYM:HEX mixtures at 1:3:26, 1:2:26, and 1:7:26 molar ratios, respectively. Separate illustrations are shown for the entire system and for the different components (red, BHT; green, MEN; blue, TYM; yellow, ChCl; gray, HEX).

mixtures with $H = 12$ (Fig. 3a and b) and $H = 26$ (Fig. 4a and b) show a rather homogeneous distribution of the components inside the simulation boxes, which is coherent with the absence of spectral features in the small-angle regime for these samples (Fig. 2a and b). On the other hand, the ChCl:TYM:HEX 1:7:12 (Fig. 3c) and 1:7:26 (Fig. 4c) systems show a clear segregation of the ChCl moiety with respect to the remaining components, suggesting that this could be at the base of the larger scale-length inhomogeneities observed from SAXS (Fig. 2c) and ultimately for the macroscopic phase separation for $H = 26$ (Figure S1c).

To validate the ability of the MD simulation to capture the formation of aggregates as those shown by the ChCl:TYM 1:7 eutectic for high HEX concentrations, in Fig. 5 we compare the experimental and MD-simulated SWAXS scattering curves for the ChCl:TYM:HEX 1:7:12 and 1:7:26 systems. A good agreement is evident in both cases, in particular for the position and amplitude of the WAXS peak, while the increasing small-angle scattering intensity previously observed in the experimental data is also remarkably well reproduced by the MD simulations. Moreover, the SWAXS spectra of the BHT:MEN:HEX 1:3:*H* and TYM:MEN:HEX 1:2:*H* systems with $H = 12$ and 26 were also calculated from the MD trajectories. As can be seen in Figure S3 and S4 there is a good agreement between the theoretical and experimental data, corroborating the reliability of the MD simulation. In particular, the simulations were able to reproduce the rather flat small-angle region for these samples, confirming the absence of structural features contributing to this spectral range.

To have a more quantitative description of these systems, site-site radial distribution functions $g(r)$'s have been computed from the MD trajectories. It is first mandatory to reconstruct the structural arrangement of the pristine eutectics, *i.e.*, for the $H = 0$ mixtures, in order to trace the structural evolution induced by HEX addition. In the case of the BHT:MEN 1:3 and TYM:MEN 1:2 eutectics, the $g(r)$'s have been calculated for all the possible intermolecular H-O combinations involving

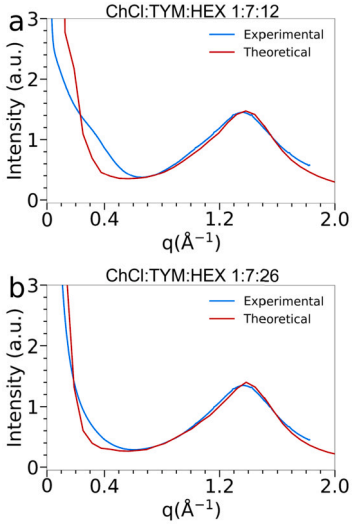

Fig. 5. Comparison between the experimental and theoretical SWAXS spectra calculated from the MD simulations for the a) ChCl:TYM:HEX 1:7:12 and b) ChCl:TYM:HEX 1:7:26 systems.

the hydroxyl groups of the constituents, as this analysis can deliver key information about the extent of H-bond aggregation. In the BHT:MEN 1:3 system, the $H_{MEN}-O_{MEN}$ distribution describing the H-bond among MEN molecules shows a distinct first peak with a maximum at 2.01 Å (Fig. 6a and Table S4). Integration of this curve up to a cutoff distance chosen at the first minimum delivers an integration number N of 0.53 (Table S4). On the other hand, the H-O distributions between BHT and MEN, as well as among BHT molecules, show poor structured peaks of negligible intensities or at considerably longer distances

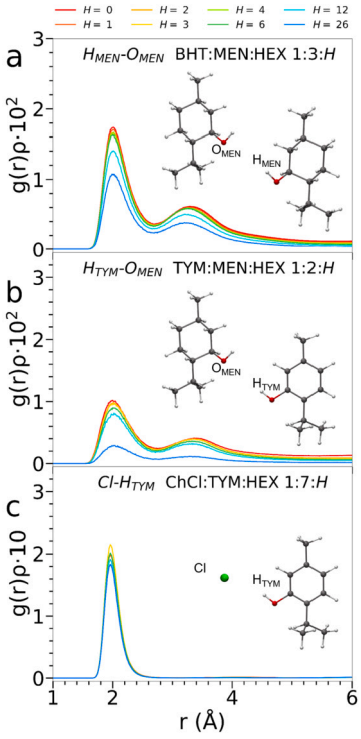

Fig. 6. Radial distribution functions multiplied by the numerical densities of the observed atoms, $g(r)\rho$'s, calculated from the MD simulations for the a) $H_{MEN}-O_{MEN}$, b) $H_{TYM}-O_{MEN}$, and c) $Cl-H_{TYM}$ distributions of the BHT:MEN:HEX, TYM:MEN:HEX, and ChCl:TYM:HEX mixtures at different 1:3:*H*, 1:2:*H*, and 1:7:*H* molar ratios.

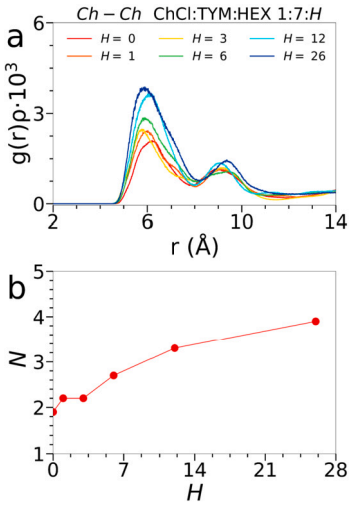

Fig. 7. a) Radial distribution functions multiplied by the numerical densities of the observed atoms, $g(r)\rho$'s, calculated for the Ch-Ch COM-COM distribution from the MD simulations for the ChCl:TYM:HEX mixtures at different 1:7:*H* molar ratios. b) Corresponding integration numbers N, calculated up to the first minimum of the $g(r)\rho$'s, plotted as a function of *H*.

(Figure S5 and Table S5-S7). This result is in agreement with previous descriptions of this eutectic, demonstrating that the MEN-MEN interaction is the strongest and possibly the only relevant H-bond in solution. [2,33,36,69] As far as the TYM:MEN 1:2 system is concerned, the $H_{TYM}-O_{MEN}$ distribution shows a first peak with a maximum at 2.00 Å and an integration number of 0.37 (Fig. 6b and Table S8). This is in agreement with previous determinations pointing to the TYM-MEN donor-receptor H-bond as the main driving force for the formation of this "type V" DES. Nevertheless, as the molar ration between the TYM and MEN components is 1:2, the excess MEN molecules are free to form H-bonds among each others, as shown by the $H_{MEN}-O_{MEN}$ distribution which is also of relevant extent, at variance with the remaining ones (Figure S6b and Table S9-S11). Finally, in the ChCl:TYM 1:7 system the most relevant interaction has been found to be the Cl-H_{TYM} one between the chloride anion and the TYM molecules (Fig. 6c and Table S12), integrating 3.12 after the first peak, while the Cl-H_{Ch} one involving the cholinium cations also integrates 0.83 at the first minimum (Figure S7a and Table S13). This shows that almost all the cholinium cations available in solution are involved in this interaction, and that the structural arrangement of the ChCl:TYM 1:7 eutectic can be described in terms of coordination shells of the chloride anion, as often found for ChCl-based DESs. [39,29,31]

After the pristine eutectics had been characterized, MD simulations were employed to unveil how the addition of the HEX cosolvent impacts on their structural arrangement. To this purpose, in Fig. 6 we report the evolution of the most relevant $g(r)$'s for increasing H values, while the same is shown in Figures S3 - S5 for the remaining pair distributions. In the BHT:MEN:HEX 1:3:*H* and TYM:MEN:HEX 1:2:*H* mixtures, the $H_{MEN}-O_{MEN}$ and $H_{TYM}-O_{MEN}$ distributions decrease in intensity for increasing H values, as also reflected by the decreasing N values listed in Tables S4 and S8. This result evidences that the introduction of the apolar cosolvent is able to disrupt the main H-bond interactions initially present in the BHT:MEN 1:3 and TYM:MEN 1:2 eutectics. As concerns the ChCl:TYM:HEX 1:7:*H* mixtures, the $Cl-H_{TYM}$ distribution does not show a clear evolution upon HEX addition, suggesting that this interaction is not key to understanding the structural changes of this eutectic. To get more insights, $g(r)$'s between the center of mass (COM) of the cholinium cations have been calculated and are shown in Fig. 7a. Here, it can be observed that the intensity of the distribution rises for increasing HEX content, as it is also evident from the evolution of the integration numbers of the first peak (Table S15) reported as a function of H in Fig. 7b. This result may subtend the increasing segregation of cholinium cations as promoted by HEX addition to the ChCl:TYM 1:7 eutectic, which could evidently be at the base of the inhomogeneities observed in the SAXS regime (Fig. 2c).

A more quantitative description of these domains has been gained from the Voronoi analysis carried out from the MD trajectories, and the results are shown in Fig. 8. The number of neighbor counts (nb counts) around a reference subset is reported in Tables S16-S20 and it is shown as a function of the mixture composition. These values correspond to the average number of neighboring contacts for a Voronoi unit, which are represented by the mixture components. In particular, the chosen criterion sees the simulation box partitioned in adjacent Voronoi cells and, if the Voronoi unit of two molecules share a common face, these are said to be neighbors. Concerning the BHT:MEN system, the nb counts between HEX and the BHT and MEN components, as well as those among HEX molecules, are found to increase along with H (Fig. 8a). At the same time, the counts among the BHT and MEN molecules decrease for increasing HEX concentration (Fig. 8b). A similar behavior is found for the TYM:MEN:HEX 1:2:*H* mixtures, where the number of contacts of the cosolvent with all the species in solution increases (Fig. 8c), while those among the TYM and MEN components decrease (Fig. 8d) for increasing HEX concentration. Altogether these results point at a higher affinity of the BHT, MEN, and TYM components towards the hydrophobic HEX cosolvent, which is at the base of the observation of no larger-scale segregation effects in the BHT:MEN:HEX and TYM:MEN:HEX mixtures. Note that the higher number of counts towards the HEX molecules displayed by the BHT:MEN 1:3 system as compared to the TYM:MEN 1:2 one, is an indication of the higher hydrophobicity of the former eutectic with respect to the latter. This finding could also explain the higher tendency to flatness of the WAXS pre-peak displayed by the BHT:MEN:HEX mixtures (Fig. 2a) with respect to the other systems (Fig. 2b and c) upon HEX addition. On the other hand, different trends can be observed for the ChCl:TYM

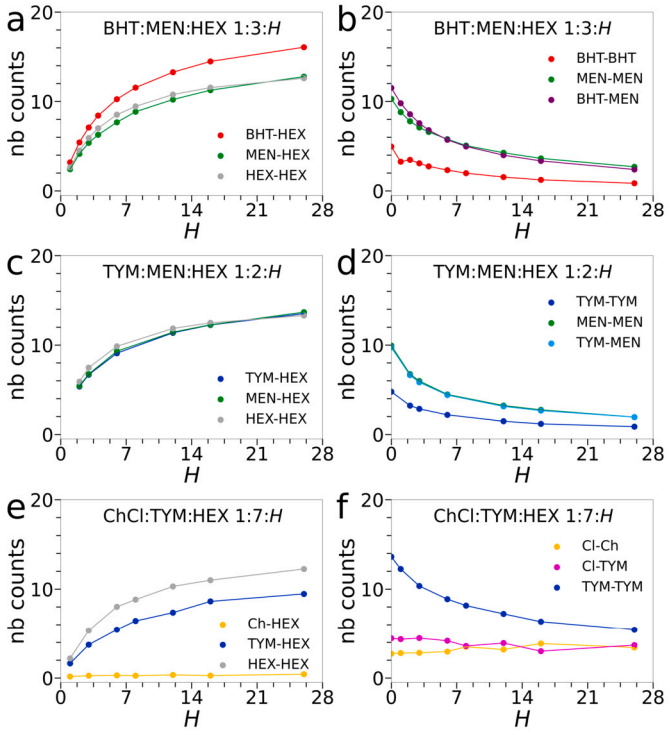

Fig. 8. Neighbor count around a reference subset calculated from the MD simulations for the BHT:MEN:HEX 1:3:*H* (a and b), TYM:MEN:HEX 1:2:*H* (c and d), and ChCl:TYM:HEX 1:7:*H* (e and f) mixtures reported as a function of *H*.

1:7 eutectic. In particular, although the TYM-HEX and HEX-HEX contacts grow for increasing *H* values, the Ch-HEX ones remain close to zero throughout the explored composition range, demonstrating that the cholinium cations hardly interact with the added cosolvent. Furthermore, the Cl-Ch and Cl-TYM counts remain rather constant across all the HEX compositions, while the TYM-TYM ones decrease (Fig. 8f). The overall result shows that, although HEX is able to interact with the TYM molecules, the smaller affinity between the apolar cosolvent and the hydrophilic ChCl is the driving force for the segregation mechanism of this component in the ChCl:TYM:HEX mixtures. Nevertheless, the large excess of the TYM compound results in the preservation of the favorable Cl-TYM interaction, also explaining the only slight perturbation of the $Cl-H_{TYM}$ $g(r)$ distribution upon HEX addition (Fig. 6c). A deeper insight into the three dimensional structural arrangement of the mixtures has been gained from the spatial distribution functions (SDFs) calculated for the BHT:MEN:HEX 1:3:12, TYM:MEN:HEX 1:2:12, and ChCl:TYM:HEX 1:7:12 systems (Figure S8). Looking at the SDFs computed around the BHT molecule in the BHT:MEN:HEX 1:3:12 system (Figure S8a) and around the TYM molecule in the TYM:MEN:HEX 1:2:12 (Figures S8c) and ChCl:TYM:HEX 1:7:12 (Figures S8f) systems, one may observe that the probability spots referred to the HEX molecules are located above and below the aromatic ring of BHT, confirming the affinity of these species for the apolar cosolvent. Similarly, it can be noticed from the SDFs calculated for the MEN molecule in the BHT:MEN:HEX 1:3:*H* and TYM:MEN:HEX 1:2:*H* mixtures (Figure S8b and S8d respectively) that the cosolvent arranges itself at the side of the alkyl chains and away from the hydroxyl group. Note that the SDFs have been drawn according to the same density/maximum ratio to properly compare different systems. Nevertheless, we remark that no probability spots were found in the SDF computed for the Ch molecule, confirming that this specie has no affinity for the HEX cosolvent, leading to the formation of inhomogeneities. The whole result confirms that the segregation mechanism of the ChCl component from the HEX cosolvent is at the base of the formation of the larger-scale inhomogeneities observed for the ChCl:TYM:HEX 1:7:12 and 1:7:26 mixtures. Note that the different behavior of these systems in front of the added cosolvent is evidently provided by the hydrophilic ChCl component, which is absent in the BHT:MEN 1:3 and TYM:MEN 1:2 eutectics. This occurs despite the low amount of ChCl in the ChCl:TYM 1:7 eutectic and shows how the formation of such aggregates is sensitive towards the nature of the components, urgently calling for a case-by-case study about the nanostructural behavior of these inherently complex systems.

4. Conclusions

The structural changes induced by the addition of an apolar cosolvent to eutectic mixtures with different degrees of hydrophobicity have been studied. SWAXS data collected on BHT:MEN:HEX, TYM:MEN:HEX, and ChCl:TYM:HEX mixtures at different molar ratios show that the introduction of the cosolvent has a similar effect on the three eutectics in terms of molecular scale-length distribution. In particular, the molecular aggregation present in the pristine eutectics is dramatically perturbed by HEX addition, as shown by the evolution of the WAXS contribution. On the other hand, the inspection of the small-angle region shows a different behavior of the three systems at a larger scale-length. While the introduction of the HEX cosolvent is translated into a homogeneous electron density distribution for the BHT:MEN:HEX and TYM:MEN:HEX mixtures, inhomogeneities at nano-scale level are shown by the ChCl:TYM:HEX system for the highest HEX contents, before macroscopic phase separation. MD simulations allowed us to elucidate the structural arrangement of the pristine eutectics, which mostly relies on H-bonding, and showed that these inter-molecular interactions are seriously perturbed in the BHT:MEN and TYM:MEN systems upon HEX addition. The high affinity of the HEX cosolvent for the BHT, MEN, and TYM species is at the base of the observation that neither phase separation nor inhomogeneities at the nano-scale level occurs even for high HEX contents. On the other hand, the presence of the more hydrophilic ChCl compound in the ChCl:TYM 1:7 eutectic is translated into a segregation of this component from the added cosolvent, which only interacts with the TYM species and with other HEX molecules. The different degree of hydrophobicity of the eutectic components is therefore key to understanding the nanostructural behavior of these systems in the presence an apolar cosolvent. Our combined SWAXS-MD approach was able to reconstruct the supramolecular picture of these mixtures, which is important for all the applications that see the presence of a cosolvent as diluted species in a DES.

CRediT authorship contribution statement

Giorgia Mannucci: Conceptualization, Data curation, Writing – original draft. **Alessandro Tofoni:** Data curation, Formal analysis. **Matteo Busato:** Conceptualization, Data curation, Writing – review & editing. **Paola D'Angelo:** Conceptualization, Data curation, Funding acquisition, Supervision, Writing – review & editing.

Declaration of competing interest

The authors declare that they have no known competing financial interests or personal relationships that could have appeared to influence the work reported in this paper.

Data availability

Data will be made available on request.

Acknowledgements

Part of the calculations was performed on the Marconi100 system of the CINECA supercomputing center (grant IsC99-CODES). The Austrian SAXS beamline of Elettra-Sincrotrone Trieste and its staff are acknowledged for synchrotron radiation beam time.

Appendix A. Supplementary material

Supplementary material related to this article can be found online at https://doi.org/10.1016/j.molliq.2023.123746.

References

[1] A.P. Abbott, G. Capper, D.L. Davies, R.K. Rasheed, V. Tambyrajah, Chem. Commun. (2003) 70–71.
[2] M. Busato, G. Mannucci, L.A. Rocchi, M.E. Di Pietro, A. Capocefalo, E. Zorzi, P. Casu, D. Veclani, F. Castiglione, A. Mele, A. Martinelli, P. Postorino, P. D'Angelo, ACS Sustain. Chem. Eng. 11 (2023) 8988–8999.
[3] D.O. Abranches, J.A. Coutinho, Curr. Opin. Green Sustain. Chem. (2022) 100612.
[4] S. Zahn, B. Kirchner, D. Mollenhauer, ChemPhysChem 17 (2016) 3354–3358.
[5] A.J. Peloquin, J.M. McCollum, C.D. McMillen, W.T. Pennington, Angew. Chem. Int. Ed. 60 (2021) 22983–22989.
[6] B.B. Hansen, S. Spittle, B. Chen, D. Poe, Y. Zhang, J.M. Klein, A. Horton, L. Adhikari, T. Zelovich, B.W. Doherty, B. Gurkan, E.J. Maginn, A. Ragauskas, M. Dadmun, T.A. Zawodzinski, G.A. Baker, M.E. Tuckerman, R.F. Savinell, J.R. Sangoro, Chem. Rev. 121 (2021) 1232–1285.
[7] M. Francisco, A. van den Bruinhorst, M.C. Kroon, Angew. Chem. 52 (2013) 3074–3085.
[8] E.L. Smith, A.P. Abbott, K.S. Ryder, Chem. Rev. 114 (2014) 11060–11082.
[9] B.D. Ribeiro, C. Florindo, L.C. Iff, M.A.Z. Coelho, I.M. Marrucho, ACS Sustain. Chem. Eng. 3 (2015) 2469–2477.
[10] D.J. van Osch, L.F. Zubeir, A. van den Bruinhorst, M.A. Rocha, M.C. Kroon, Green Chem. 17 (2015) 4518–4521.
[11] D.O. Abranches, M.A. Martins, L.P. Silva, N. Schaeffer, S.P. Pinho, J.A. Coutinho, Chem. Commun. 55 (2019) 10253–10256.
[12] N. Schaeffer, D.O. Abranches, L.P. Silva, M.A. Martins, P.J. Carvalho, O. Russina, A. Triolo, L. Paccou, Y. Guinet, A. Hedoux, J.A. Coutinho, ACS Sustain. Chem. Eng. 9 (2021) 2203–2211.
[13] P. Makoś, E. Słupek, J. Gębicki, Microchem. J. 152 (2020) 104384.
[14] Y. Dai, G.-J. Witkamp, R. Verpoorte, Y.H. Choi, Food Chem. 187 (2015) 14–19.
[15] N. López-Salas, J.M. Vicent-Luna, S. Imberti, E. Posada, M.J. Roldán, J.A. Anta, S.R.G. Balestra, R.M. Madero Castro, S. Calero, R.J. Jiménez-Riobóo, M.C. Gutiérrez, M.L. Ferrer, F. del Monte, ACS Sustain. Chem. Eng. 7 (2019) 17565–17573.
[16] P. Tomai, A. Lippiello, P. D'Angelo, I. Persson, A. Martinelli, V. Di Lisio, R. Curini, C. Fanali, A. Gentili, J. Chromatogr. A 1605 (2019) 360329.
[17] V. Gallo, P. Tomai, M. Gherardi, C. Fanali, L. De Gara, G. D'Orazio, A. Gentili, J. Chromatogr. A 1642 (2021) 462036.
[18] P. Tomai, A. Gentili, R. Curini, R. Gottardo, Franco Tagliaro, S. Fanali, J. Pharm. Anal. 11 (2021) 292–298.
[19] F. Gabriele, M. Chiarini, R. Germani, M. Tiecco, N. Spreti, J. Mol. Liq. 291 (2019) 111301.
[20] Y. Wang, C. Ma, C. Liu, X. Lu, X. Feng, X. Ji, J. Chem. Eng. Data 65 (2020) 2446–2457.
[21] X. Meng, K. Ballerat-Busserolles, P. Husson, J.-M. Andanson, New J. Chem. 40 (2016) 4492–4499.
[22] A.R. Harifi-Mood, R. Buchner, J. Mol. Liq. 225 (2017) 689–695.
[23] Y. Xie, H. Dong, S. Zhang, X. Lu, X. Ji, J. Chem. Eng. Data 59 (2014) 3344–3352.
[24] R. Alcalde, M. Atilhan, S. Aparicio, J. Mol. Liq. 272 (2018) 815–820.
[25] N.F. Gajardo-Parra, M.J. Lubben, J.M. Winnert, Á. Leiva, J.F. Brennecke, R.I. Canales, J. Chem. Thermodyn. 133 (2019) 272–284.
[26] S.J. Bryant, A.J. Christofferson, T.L. Greaves, C.F. McConville, G. Bryant, A. Elbourne, J. Colloid Interface Sci. 608 (2022) 2430–2454.
[27] A. Elbourne, N. Meftahi, T.L. Greaves, C.F. McConville, G. Bryant, S.J. Bryant, A.J. Christofferson, Adv. Colloid Interface Sci. 591 (2021) 38–51.
[28] O.S. Hammond, D.T. Bowron, K.J. Edler, Angew. Chem. Int. Ed. 56 (2017) 9782–9785.
[29] O.S. Hammond, D.T. Bowron, A.J. Jackson, T. Arnold, A. Sanchez-Fernandez, N. Tsapatsaris, V. Garcia Sakai, K.J. Edler, J. Phys. Chem. B 121 (2017) 7473–7483.
[30] M. Busato, V. Di Lisio, A. Del Giudice, P. Tomai, V. Migliorati, L. Galantini, A. Gentili, A. Martinelli, P. D'Angelo, J. Mol. Liq. 331 (2021) 115747.
[31] M. Busato, V. Migliorati, A. Del Giudice, V. Di Lisio, P. Tomai, A. Gentili, P. D'Angelo, Phys. Chem. Chem. Phys. 23 (2021) 11746–11754.
[32] M. Busato, A. Del Giudice, V. Di Lisio, P. Tomai, V. Migliorati, A. Gentili, A. Martinelli, P. D'Angelo, ACS Sustain. Chem. Eng. 9 (2021) 12252–12261.
[33] M. Busato, G. Mannucci, V. Di Lisio, A. Martinelli, A. Del Giudice, A. Tofoni, C. Dal Bosco, V. Migliorati, A. Gentili, P. D'Angelo, ACS Sustain. Chem. Eng. 10 (2022) 6337–6345.
[34] G. Mannucci, M. Busato, A. Tofoni, P. D'Angelo, J. Mol. Liq. 375 (2023) 121302.
[35] D.J.G.P. van Osch, C.H.J.T. Dietz, J. van Spronsen, M.C. Kroon, F. Gallucci, M. van Sint Annaland, R. Tuinier, ACS Sustain. Chem. Eng. 7 (2019) 2933–2942.
[36] C. Dal Bosco, V. Di Lisio, P. D'Angelo, A. Gentili, ACS Sustain. Chem. Eng. 9 (2021) 8170–8178.
[37] C. Dal Bosco, F. Mariani, A. Gentili, Molecules 27 (2022) 908.
[38] M.K. Rajput, M. Konwar, D. Sarma, Water Environ. Res. 93 (2021) 2250–2260.
[39] V. Migliorati, F. Sessa, P. D'Angelo, Chem. Phys. Lett. X 2 (2019) 100001.
[40] S. Spittle, D. Poe, B. Doherty, C. Kolodziej, L. Heroux, M.A. Haque, H. Squire, T. Cosby, Y. Zhang, C. Fraenza, S. Bhattacharyya, M. Tyagi, J. Peng, R. Elgammal, T. Zawodzinski, M. Tuckerman, S. Greenbaum, B. Gurkan, C. Burda, J. Sangoro, Nat. Commun. 13 (2022) 219.
[41] P. Kumari Shobhna, S. Kaur, H.K. Kashyap, ACS Omega 3 (2018) 15246–15255.
[42] S. Kaur, M. Kumari, H.K. Kashyap, J. Phys. Chem. B 124 (2020) 10601–10616.
[43] S. Kaur, A. Gupta, H.K. Kashyap, J. Phys. Chem. B 124 (2020) 2230–2237.
[44] S. Kaur, A. Malik, H.K. Kashyap, J. Phys. Chem. B 123 (2019) 8291–8299.
[45] A. Malik, H.K. Kashyap, J. Chem. Phys. 155 (2021) 044502.
[46] A. Malik, H.K. Kashyap, Phys. Chem. Chem. Phys. 25 (2023) 19693–19705.
[47] M. Busato, A. Tofoni, G. Mannucci, F. Tavani, A. Del Giudice, A. Colella, M. Giustini, P. D'Angelo, Inorg. Chem. 61 (2022) 8843–8853.
[48] R. Haider, B. Sartori, A. Radeticchio, M. Wolf, S. Dal Zilio, B. Marmiroli, H. Amenitsch, J. Appl. Crystallogr. 54 (2021) 132–141.
[49] M. Sztucki, T. Narayanan, J. Appl. Crystallogr. 40 (2007) s459–s462.
[50] L. Martínez, R. Andrade, E. Birgin, J. Martínez, J. Comput. Chem. 30 (2009) 2157–2164.
[51] W.L. Jorgensen, D.S. Maxwell, J. Tirado-Rives, J. Am. Chem. Soc. 118 (1996) 11225–11236.
[52] J.N. Canongia Lopes, A.A. Pádua, J. Phys. Chem. B 108 (2004) 16893–16898.
[53] J.N. Canongia Lopes, A.A. Pádua, J. Phys. Chem. B 110 (2006) 19586–19592.
[54] M. Jasik, B. Szefczyk, J. Mol. Model. 22 (2016) 1–9.
[55] T. Darden, D. York, L. Pedersen, J. Chem. Phys. 98 (1993) 10089–10092.
[56] U. Essmann, L. Perera, M.L. Berkowitz, T. Darden, H. Lee, L.G. Pedersen, J. Chem. Phys. 103 (1995) 8577–8593.
[57] F. Sessa, V. Migliorati, A. Serva, A. Lapi, G. Aquilanti, G. Mancini, P. D'Angelo, Phys. Chem. Chem. Phys. 20 (2018) 2662–2675.
[58] M. Busato, A. Lapi, P. D'Angelo, A. Melchior, J. Phys. Chem. B 125 (2021) 6639–6648.
[59] M. Busato, P. D'Angelo, A. Lapi, M. Tolazzi, A. Melchior, J. Mol. Liq. 299 (2020) 112120.
[60] M. Busato, P. D'Angelo, A. Melchior, Phys. Chem. Chem. Phys. 21 (2019) 6958–6969.
[61] A. Abbott, H. Abe, L. Aldous, R. Atkin, M. Bendová, M. Busato, J.N. Canongia Lopes, M. Costa Gomes, B. Cross, C. Dietz, J. Everts, M. Firestone, R. Gardas, M. Gras, T. Greaves, S. Halstead, C. Hardacre, J. Harper, J. Holbrey, J. Jacquemin, P. Jessop, D. MacFarlane, F. Maier, H. Medhi, M. Mezger, A. Pádua, S. Perkin, J.E.S.J. Reid, S. Saha, J.M. Slattery, M.L. Thomas, S. Tiwari, S. Tsuzuki, B. Uralcan, M. Watanabe, J. Wishart, T. Youngs, Faraday Discuss. 206 (2018) 113–139.
[62] B. Hess, H. Bekker, H.J. Berendsen, J.G. Fraaije, J. Comput. Chem. 18 (1997) 1463–1472.
[63] M.J. Abraham, T. Murtola, R. Schulz, S. Páll, J.C. Smith, B. Hess, E. Lindahl, SoftwareX 1 (2015) 19–25.
[64] M. Brehm, H. Weber, M. Thomas, O. Hollóczki, B. Kirchner, ChemPhysChem 16 (2015) 3271–3277.
[65] M. Brehm, B. Kirchner, TRAVIS-a Free Analyzer and Visualizer for Monte Carlo and Molecular Dynamics Trajectories, 2011.
[66] D.T. Cromer, J.B. Mann, Acta Crystallogr., Sect. A 24 (1968) 321–324.
[67] W. Humphrey, A. Dalke, K. Schulten, J. Mol. Graph. 14 (1996) 33–38.
[68] A. Malik, H.K. Kashyap, Phys. Chem. Chem. Phys. 23 (2021) 3915–3924.
[69] M. Busato, G. Mannucci, V. Di Lisio, A. Martinelli, A. Del Giudice, A. Tofoni, C. Dal Bosco, V. Migliorati, A. Gentili, P. D'Angelo, ACS Sustain. Chem. Eng. 10 (2022) 8671–8672.